文章编号：1001－9014(2017)03－0270－06

DOI:10.11972/j.issn.1001－9014.2017.03.004

Weak antilocalization effect in Tellurium-doped Bi_2Se_3 topological insulator nanowires

TIAN Feng[1,2], ZHOU Yuan-Ming[1,2*], ZHANG Xiao-Qiang[3], WEI Lai-Ming[3], MEI Fei[1,2], XU Jin-Xia[1,2], JIANG Yan[1,2], WU Lin-Zhang[2], KANG Ting-Ting[4], YU Guo-Lin[4*]

(1. Hubei Collaborative Innovation Center for High-efficiency Utilization of Solar Energy, Hubei University of Technology, Wuhan 430068, China;
2. School of Electrical and Electronic Engineering, Hubei University of Technology, Wuhan 430068, China;
3. Hefei National Laboratory for Physical Sciences at the Microscale, University of Science and Technology of China, Hefei 230026, China;
4. National Laboratory for Infrared Physics, Shanghai Institute of Technical Physics, Chinese Academy of Sciences, Shanghai 200083, China)

Abstract: Single-crystalline Bi_2Se_3 and $Bi_2(Te_xSe_{1-x})_3$ nanowires were synthesized via Au catalytic vapor-liquid-solid (VLS) growth method. Electronic properties of the surface states in individual $Bi_2(Te_xSe_{1-x})_3$ ($x=0.26$) nanowire were studied by low-temperature magnetotransport measurement. Weak antilocalization (WAL) effect was found, suggesting strong spin-orbit coupling in our samples. It is indicated that the bulk effect can be suppressed effectively by the Tellurium (Te) doping. By fitting the magnetoconductance curves at magnetic field up to 7 T measured at different temperatures, the extracted dephasing length l_φ decreases from 389 nm at 1.5 K to 39 nm at 20 K, which can be well described by the power law $l_\varphi \propto T^{-0.96}$. It can be reasonably deduced that both the electron-electron scattering and the electron-phonon scattering play important roles in the Te-doped sample.

Key words: topological insulator, Bi_2Se_3 nanowires, weak antilocalization, dephasing length

PACS: 73.20Fz, 72.25.Dc

Te元素掺杂 Bi_2Se_3 拓扑绝缘体纳米线的反弱局域效应

田 锋[1,2], 周远明[1,2*], 张小强[3], 魏来明[3], 梅 菲[1,2], 徐进霞[1,2], 蒋 妍[1,2], 吴麟章[2], 康亭亭[4], 俞国林[4*]

(1. 湖北工业大学 太阳能高效利用湖北省协同创新中心,湖北 武汉 430068;
2. 湖北工业大学 电气与电子工程学院,湖北 武汉 430068;
3. 中国科学技术大学合肥微尺度物质科学国家实验室,安徽 合肥 230026;
4. 中国科学院上海技术物理研究所 红外物理国家重点实验室,上海 200083)

摘要:采用Au催化的固-液-气(VLS)方法制备了单晶 Bi_2Se_3 和 $Bi_2(Te_xSe_{1-x})_3$ 纳米线,研究了单根纳米线器件的输运性质.在对单根 $Bi_2(Te_xSe_{1-x})_3$ ($x=0.26$) 纳米线的低温磁输运测试中观察到反弱局域效应,说明样品中存在较强的自旋-轨道耦合.结果表明,Te掺杂可以有效抑制体电导对输运过程的影响.通过对不同温度下的磁电导曲线进行拟合,得到了电子的退相干长度 l_φ,l_φ 从1.5 K时的389 nm减小至20 K时的39 nm,遵循 $l_\varphi \propto T^{-0.96}$ 指数变化规律.分析表明,在Te掺杂样品的输运过程中,电子-电子散射和电子-声子散射均起到了十分重要的作用.

Received date: 2016-11-12, **revised date**: 2017-01-05　　**收稿日期**:2016-11-12, **修回日期**:2017-01-05

Foundation items: Supported by the National Natural Science Foundation of China (11304092, 51371079, 11305056, 11304299, 51602099); the Open Foundation of Hubei Collaborative Innovation Center for High-efficiency Utilization of Solar Energy (HBSKFZD2014001, HBSKFM2014006, HBSKFM2014013, HBSKFM2014015)

Biography: TIAN Feng (1990-), male, Wuhan, master. Research area involves Semiconductor materials and devices. E-mail: tifen2010@126.com

* **Corresponding author**: E-mail: ymzhou@mail.sitp.ac.cn; yug@mail.sitp.ac.cn

关　键　词: 拓扑绝缘体; Bi_2Se_3 纳米线; 反弱局域; 退相干长度

中图分类号: O484.3　　**文献标识码**: A

Introduction

Bi_2Se_3 topological insulator (TI) is a novel quantum material with an insulating bulk band and gapless metallic surface states that are protected by time-reversal symmetry[1-2]. In this material, surface states show large spin-orbit coupling (SOC), and are protected against any time reversal perturbations, such as back scattering and crystal defects. These unique properties make Bi_2Se_3 to be a promising material in spintronics, quantum information and low-energy dissipation electronics. However, due to the large bulk conductivity caused by Selenium (Se) vacancies in Bi_2Se_3, it is hard to distinguish whether the electronic properties measured by transport experiments are originated from the surface states or the bulk states, making it difficult to study the intrinsic properties of surface states in Bi_2Se_3 topological insulator.

As reported in earlier literatures, several methods have been tried to suppress the bulk effect, i. e., substitutional doping in order to decrease the bulk conductivity directly [3-7], and preparing Bi_2Se_3 nanostructures which can increase the surface-to-volume ratio[8-14]. On the one hand, the substitutional doping using various dopants like Ca[3], Sb[4], and Te[5-7] has been studied and shows promise for reducing the bulk carrier density in Bi_2Se_3 bulk crystals. Furthermore, the increased mobility made some quantum transport phenomena to be observed easily, such as Shubnikov-de Haas (SdH) oscillations[4-7]. For example, Cava and Ong found that the resistivity of Bi_2Te_2Se single crystal could reach the maximum of 6 Ω · cm, the surface electron mobility ($\sim$2 800 cm^2/Vs) was much larger than the bulk electron mobility ($\sim$50 cm^2/Vs), and the SdH oscillations were observed in 14 T magnetic field[6-7]. All of these studies proposed that the observed SdH oscillations mainly came from the contribution of the surface states and suggested the bulk conductance could be effectively suppressed by doping. On the other hand, some groups prepared Bi_2Se_3 nanostructures in order to suppress the bulk effect and found some quantum transport phenomena[8-14]. For example, the Cui's group successfully prepared several kinds of Bi_2Se_3 nanostructures[8-12], in which both the SdH oscillations and weak antilocalization (WAL) effect were found in $(Bi_{1-x}Sb_x)Se_3$ nanoribbons[11], while only the WAL effect was observed in $Bi_2(Se_xTe_{1-x})_3$ nanorribons and nanoplates[12]. As we know, there are little literatures focusing on the doped topological insulator nanostructures and the related work needs to be done further.

In this study, we synthesized Bi_2Se_3 and $Bi_2(Te_xSe_{1-x})_3$ nanowires via Au catalytic vapor-liquid-solid (VLS) growth method. The low-temperature magnetotransport measurement was employed to study the electronic properties of the surface state in $Bi_2(Te_xSe_{1-x})_3$ nanowires. The WAL effect is clearly observed and analyzed in this paper.

1　Experiments

The highly single-crystalline Bi_2Se_3 and $Bi_2(Te_xSe_{1-x})_3$ nanowires were synthesized by a simple chemical vapor deposition (CVD) in a horizontal tube furnace (MTI, OTF-1200X) equipped with a 1 inch-diameter quartz tube. There are two commercial materials as evaporating sources, namely, Bi_2Se_3 powders (99.999%, from Alfa Aesar) were placed into the hot center of the tube, while Bi_2Te_3 powders (99.999%, from Alfa Aesar) were placed in the upstream zone of the tube with a distance of 20 cm away from the center. The growth substrate (Si substrate with 300 nm SiO_2 layer) coated with 1 nm thick Au film was placed downstream at 21.5 cm distance from the center in order to collect the products. Before the growth, the tube was initially pumped to 10 mTorr by mechanical pump and flushed with ultrapure Ar gas repeatedly more than three times to remove O_2 residue. Then, the furnace was heated accurately to 540℃ at a rate of 20℃ /min and kept the temperature for 1.5 h under 80 sccm Ar carrier gas flow, while the pressure in the tube was maintained at $\sim$130 Pa. After the reaction completed, the furnace was cooled naturally to room temperature. A gray coating layer covering the substrate indicates the existence of $Bi_2(Te_xSe_{1-x})_3$ nanomaterials. The similar method was employed to synthesize Bi_2Se_3 nanowires with removing the Bi_2Te_3 powders.

The structure information of the as-grown products was determined using X-ray diffraction (XRD, Bruker D8 Advance). The morphology and chemical stoichiometry of the sample were characterized by scanning electron microscopy (SEM, PHILIPS XL30 TMP) equipped with energy dispersive X-ray (EDX) spectroscopy. The crystallinity and orientation of the sample were obtained from the images of high-resolution transmission electron microscope (HRTEM, FEI TECNAI G2 20) and selected area electron diffraction patterns (SAED) operated at 200 kV.

For device fabrication and transport measurements, the synthesized Bi_2Se_3 and $Bi_2(Te_xSe_{1-x})_3$ nanowires were mechanically transferred onto a fresh Si substrate with 300 nm SiO_2 layer. Using a standard e-beam lithography technique, multi-terminal electrodes were patterned on individual Bi_2Se_3 and $Bi_2(Te_xSe_{1-x})_3$ nanowires. With e-beam evaporation of Ti/Au (10/90 nm) and standard lift-off processes, the devices were fabricated and then measured via magnetotransport measurements, which were performed in a no helium cryostat system (Oxford Instruments) with a base temperature of 1.5 K, equipped with an 8 T magnet. The magnetic field up to 7 T was applied perpendicular to the substrate plane. The electrical signals were measured using low-frequency lock-in techniques.

2 Results and discussions

The crystal structure of Bi_2Se_3 and $Bi_2(Te_xSe_{1-x})_3$ nanowires can be confirmed by XRD measurements directly on the as-grown substrates due to the large yield. As shown in Fig. 1, the XRD pattern of the undoped sample suggests the rhombohedral structure of Bi_2Se_3 with lattice constants a = 0.414 nm and c = 2.864 nm (PDF#00-033-0214), which is the typical characteristic of single-phase Bi_2Se_3. While for the $Bi_2(Te_xSe_{1-x})_3$ nanowires, the XRD peaks show a little shift to the small-angle direction, and keeps the single-phase rhombohedral structure.

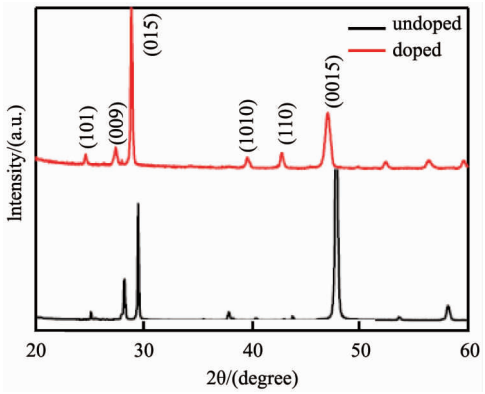

Fig. 1 XRD patterns of Bi_2Se_3 and $Bi_2(Te_xSe_{1-x})_3$ nanowires
图1 Bi_2Se_3 和 $Bi_2(Te_xSe_{1-x})_3$ 纳米线的 XRD 图谱

Figures 2(a) and (c) show typical scanning electron microscopy (SEM) images of Bi_2Se_3 and $Bi_2(Te_xSe_{1-x})_3$ nanowires, respectively. The widths of nanowires are several hundred nanometers, while the lengths are up to several tens of micrometers. For the device measurements in this paper, the widths of the individual Bi_2Se_3 and $Bi_2(Te_xSe_{1-x})_3$ nanowires are 122 nm and 222 nm, respectively. As clearly seen in the high-magnification SEM images, the presence of Au nanoparticle at the end of each nanowire suggests the VLS growth mechanism. As shown in Figs. 2(b) and (d), the EDX analysis reveals that the atomic ratio of Bi:Se is approximately equal to 2:3 for the undoped sample, demonstrating that the synthesized nanowires are indeed Bi_2Se_3, while the doping concentration is determined to be x = 0.26 for the Te-doped sample.

Figure 3(a) is a typical low-magnification transmission electron microscopy (TEM) image of an individual $Bi_2(Te_xSe_{1-x})_3$ nanowire. The corresponding selected area electron diffraction (SAED) exhibits a clear hexagonally symmetric spots pattern, confirming that the $Bi_2(Te_xSe_{1-x})_3$ nanowire is single crystalline and grows along the $[11\bar{2}0]$ direction. Figure 3(b) shows the high-resolution TEM (HRTEM) image of the same nanowire, which reveals expected hexagonal lattice fringes with a lattice spacing of 0.21 nm, consistent with the lattice spacing between $(11\bar{2}0)$ planes.

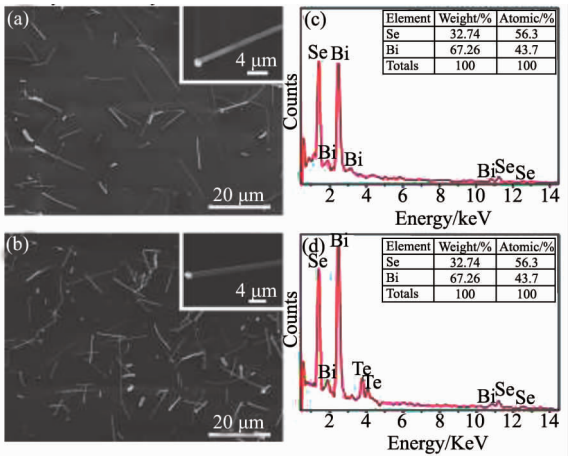

Fig. 2 (a) SEM image and (b) EDX spectrum of Bi_2Se_3 nanowires. The inset of b shows that the atomic ratio of Bi:Se is 2:3. (c) SEM image and (d) EDX spectrum of $Bi_2(Te_xSe_{1-x})_3$ nanowires. The inset of (d) shows that the doping concentration x = 0.26
图2 (a-b) Bi_2Se_3 纳米线的 SEM 图像和 EDX 图谱,图 b 中的插图为 Bi、Se 的质量百分比和原子百分比,结果表明 Bi、Se 的原子数比例为 2:3. (c-d) $Bi_2(Te_xSe_{1-x})_3$ 纳米线的 SEM 图像和 EDX 图谱,图 d 中的插图为 Bi、Se、Te 的质量百分比和原子百分比,结果表明 Te 掺杂浓度 x = 0.26

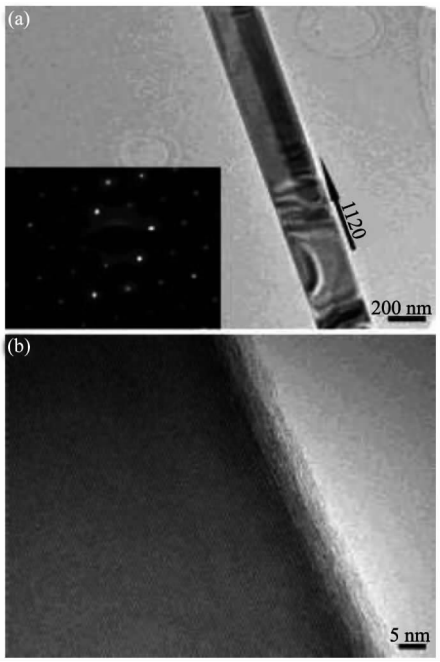

Fig. 3 (a) Low-magnification TEM image and SAED pattern of individual $Bi_2(Te_xSe_{1-x})_3$ nanowire. (b) High-resolution TEM image of $Bi_2(Te_xSe_{1-x})_3$ nanowire
图3 (a)单根 $Bi_2(Te_xSe_{1-x})_3$ 纳米线的低倍 TEM 图像和选区电子衍射花样. (b)单根 $Bi_2(Te_xSe_{1-x})_3$ 纳米线的高倍 TEM 图像

The magnetoresistance (MR) measurements provide efficient means to probe the transport properties of TIs.

Figure 4 (a) displays the normalized MR of different samples measured at T = 1.5 K in a magnetic field perpendicular to the substrate. In the undoped sample, MR shows a steep increase at low field with the change nearly same to that found in the doped sample, indicating the presence of weak antilocalization (WAL) effect. While in the high field regime, the MR evolves into a parabolic B^2 dependence, which was considered as a bulk-dominated effect[15-19]. It means that the contribution from the bulk states becomes pronounced in the high-field regime. Furthermore, it is clear that the parabolic contribution becomes much smaller in the Te-doped sample, reflecting the decreased weight of bulk MR. Thus, it is reasonable to conclude that the bulk effect can be suppressed effectively by Te doping in our samples. In the next section, we will focus on the electronic properties of the Te-doped sample. Figure. 4(b) shows the normalized MR of the Te-doped sample at different temperatures. On increasing the temperature, the MR dip in low-field regime is broadened gradually and finally disappears due to the decrease of the dephasing length at higher T. As shown in the inset of Fig. 4(b), the resistance decreases with changing temperature from 80 K to ~20 K and saturates at lower T, showing a typical metallic behavior[11, 19].

Figure 5(a) shows the magnetoconductance (MC) curves of the Te-doped nanowire measured at different temperatures, which can be used to study the dependence of the dephasing length on temperature, and thus the dephasing mechanism. As expected, the WAL effect becomes weaker and finally disappears at higher temperatures due to the decrease of the dephasing length caused by increased thermal scattering. This WAL effect is the result of strong spin-orbit coupling, which makes backscattering at the minimum in zero magnetic field, due to the time-reversal symmetry. On increasing the magnetic field, the time-reversal symmetry is broken and backscattering increases, which leads to sharp reduction in conductance. In 2D case, the correction to the low-field magnetoconductance, $\Delta\sigma(B)=\sigma(B)-\sigma(0)$, can be well described by the standard Hikami-Larkin-Nagaoka (HLN) theory for WAL[20]:

$$\Delta\sigma = -\alpha\frac{e^2}{2\pi^2 h}\left[\ln\frac{\hbar}{4Bel_\varphi^2}-\psi\left(\frac{1}{2}+\frac{\hbar}{4Bel_\varphi^2}\right)\right] \quad , \quad (1)$$

where $\hbar$ is Planck's constant, l_φ is the dephasing length, and $\psi(x)$ is the digamma function. The value of α provides information about the nature of the carriers in TIs. By fitting the low-field MC curves with the HLN theory, the obtained α value is determined to be in the range from -1.3 to -1.8, suggesting strong spin-orbit coupling. Figure 5(b) shows the extracted values of l_φ, which can be well fitted by the power law $l_\varphi \propto T^{-0.98}$. The l_φ value decreases from 290 nm in 1.5 K to 31 nm in 20 K, which can be attributed to the inelastic scattering, i.e., electron-electron scattering or electron-phonon scattering.

As reported in Ref. [12], different B-range for the WAL fits may affect the extracted l_φ value. In order to determine the above results, the total correction to the magnetoconductance $\Delta\sigma$ in the full B range of 0 ~ 7 T was fitted by the combination of the WAL effect $\Delta\sigma^{WAL}$,

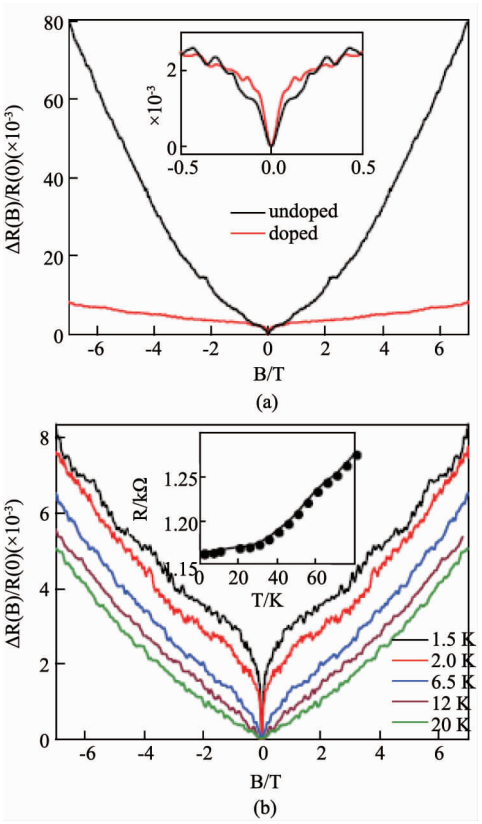

Fig. 4　(a) The magnetic field dependence of normalized magnetoresistance (defined as (R(B)-R(0))/R(0)) at 1.5 K of undoped (red line) and doped (dark line) samples, respectively. Inset is the zoomed-in view near zero field showing robustness of the WAL effect. (b) The magnetic field dependence of normalized magnetoresistance of the Te-doped sample at different temperatures. Inset is the temperature dependence of the resistance at zero magnetic field in the range of 1.5 ~ 80 K

图 4　(a) 1.5 K 时掺杂样品(红线)和未掺杂样品(黑线)的归一化磁电阻实验曲线,插图为零磁场附近的放大图. (b) 不同温度下 Te 掺杂样品的归一化磁电阻实验曲线,插图为电阻随温度的变化曲线

which dominates in the low-filed regime, and classical Drude conductance $\Delta\sigma^D$, which plays important role in the high-filed regime[21-22]:

$$\begin{aligned}\Delta\sigma &= \Delta\sigma^{WAL}+\Delta\sigma^{D}\\ &= -\alpha\frac{e^2}{2\pi^2\hbar}\left[\ln\frac{\hbar}{4Bel_\varphi^2}-\psi\left(\frac{1}{2}+\frac{\hbar}{4Bel_\varphi^2}\right)\right]\\ &\quad + ne\mu\left(\frac{1}{1+\mu^2B^2}-1\right) \quad , \quad (2)\end{aligned}$$

where n is the electron concentration and μ is the electron mobility. The obtained α value is in the range from -0.9 to -1.3. As well known, $\alpha = -1/2$ corresponds to a single surface state, while $\alpha = -1$ is attributed to two surface states, i.e., top and bottom surfaces[12, 18-19]. It means that the WAL effect in this paper originates from the two surface states. The extracted l_φ value decreases from 389 nm in 1.5 K to 39 nm in 20 K, which can be well described by the power law $l_\varphi \propto T^{-0.96}$. Although the l_φ values are larger than the results obtained by analyzing

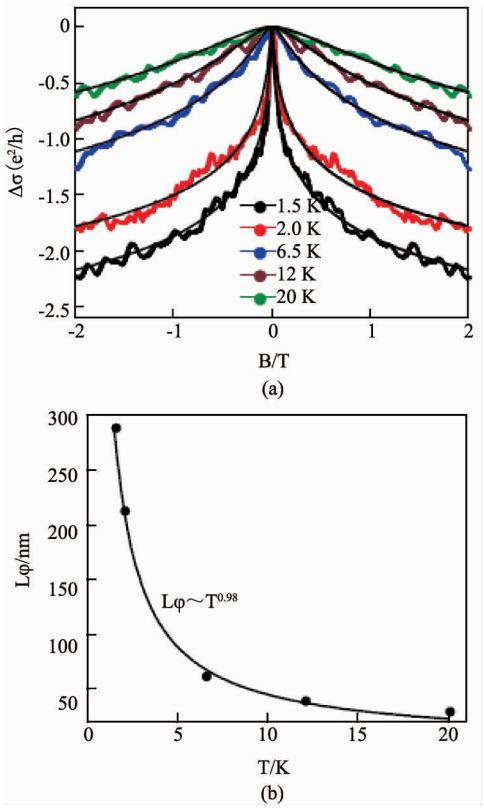

Fig. 5 (a) The low magnetic field dependence of normalized magnetoconductance of the Te-doped sample at different temperatures. The solid lines are the fitted curves with the HLN theory in the B range of 0 ~ 2 T. (b) l_φ as a function of temperature obtained from fitting the magnetoconductance with the HLN theory. The solid lines show the power-law dependence on temperature

图5 (a)不同温度下 Te 掺杂样品的归一化低场磁电导实验曲线,实线为 0 ~ 2 T 磁场范围的拟合曲线.(b)采用 HLN 理论拟合磁电导曲线得到的电子退相干长度 l_φ 随温度的变化曲线,实线为拟合曲线,表明 l_φ 随温度呈指数变化

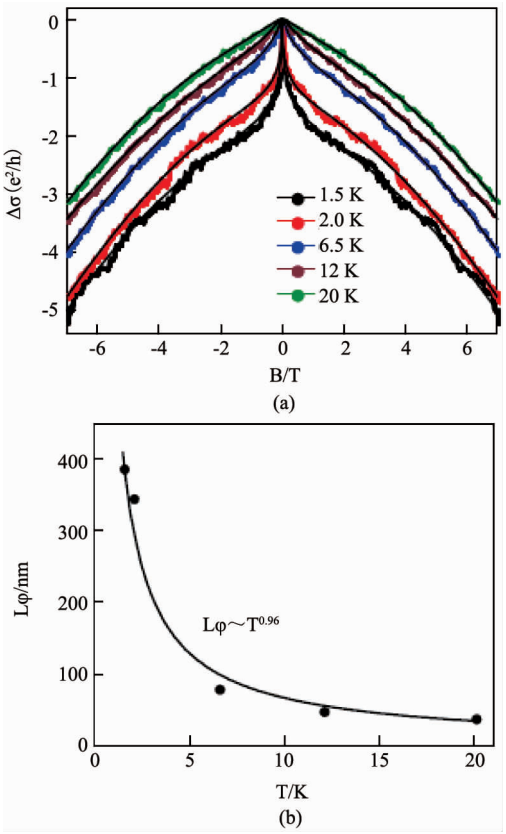

Fig. 6 (a) The magnetic field dependence of normalized magnetoconductance of the Te-doped sample at different temperatures. The solid lines are the fitted curves with the Eq. 2 in the B range of 0 ~ 7 T. (b) The fitted l_φ value as a function of temperature. The solid lines show the power-law dependence on temperature

图6 (a)不同温度下 Te 掺杂样品的归一化磁电导实验曲线,实线为 0 ~ 7 T 磁场范围的拟合曲线.(b)采用式(2)拟合磁电导曲线得到的电子退相干长度 l_φ 随温度的变化曲线,实线为拟合曲线,表明 l_φ 随温度呈指数变化

the low-field magnetoconductance, the exponent of -0.96 is well consistent with the above value of -0.98. For electron-electron scattering in 2D case, the power law dependence should be $l_\varphi \propto T^{-1/2}$, while for scattering in 3D, it is $T^{-3/4}$[23-24]. Both two exponents are smaller than our result, and thus only the electron-electron scattering can not explain the phenomenon in this paper. It is noted that, for electron-phonon interaction, the power law dependence is $l_\varphi \propto T^{-3/2}$[25-26]. It can be reasonably deduced that both the electron-electron scattering and the electron-phonon scattering play important roles in the Te-doped sample. We can also roughly estimate the values of n and μ to be $\sim 1.1 \times 10^{13}$ cm^{-2} and ~ 450 cm^{2}V^{-1}s^{-1} respectively, which are comparable to the earlier literature[11].

3 Conclusions

In summary, we studied the transport properties of single-crystalline Bi_2Se_3 and $Bi_2(Te_xSe_{1-x})_3$ nanowires synthesized via Au catalytic vapor-liquid-solid (VLS) growth method. The dopant Bi_2Te_3 was employed to replace the Selenium (Se) site with Tellurium (Te) and increase the resistivity of the bulk state, finally suppressing the contribution from the bulk electrons. According to the EDX analysis, the Te-doping concentration is $x = 0.26$. Low-temperature magnetotransport measurement was employed to study the electronic properties of the surface states in individual $Bi_2(Te_xSe_{1-x})_3$ nanowire, and the WAL effect was clearly observed. The bulk effect can be suppressed effectively by the Te doping. The obtained α value is in the range from -0.9 to -1.3, suggesting strong spin-orbit coupling. By fitting the magnetoconductance curves in the full B-range of 0 ~ 7 T measured in different temperatures, the dephasing length l_φ decreases from 389 nm in 1.5 K to 39 nm in 20 K, which can be well fitted by the power law $l_\varphi \propto T^{-0.96}$. We deduced that

both the electron-electron scattering and the electron-phonon scattering play important roles in the Te-doped sample.

References

[1] Hasan M Z, Kane C L. Colloquium: topological insulators [J]. *Reviews of Modern Physics*, 2010, **82**: 3045 - 3067.

[2] Qi X L, Zhang S C. Topological insulators and superconductors [J]. Reviews of Modern Physics, 2011, **83**: 1057 - 1110.

[3] Hsieh D, Xia Y, Qian D, *et al*. A tunable topological insulator in the spin helical Dirac transport regime [J]. *Nature*, 2009, **460**: 1101 - 1105.

[4] Analytis J G, McDonald R D, Riggs S C, *et al*. Two-dimensional surface state in the quantum limit of a topological insulator [J]. *Nature Physics*, 2010, **6**: 960 - 964.

[5] Ren Z, Taskin A A, Sasaki S, *et al*. Large bulk resistivity and surface quantum oscillations in the topological insulator Bi_2Te_2Se [J]. *Physical Review B*, 2010, **82**: 241306.

[6] Xiong J, Petersen A C, Qu D X, *et al*. Quantum oscillations in a topological insulator Bi_2Te_2Se with large bulk resistivity (6 Ω · cm) [J]. *Physica E*, 2012, **44**: 917 - 920.

[7] Xiong J, Luo Y K, Khoo Y H, *et al*. High-field Shubnikov - de Haas oscillations in the topological insulator Bi_2Te_2Se [J]. *Physical Review B*, 2012, **86**: 045314.

[8] Peng H L, Lai K J, Kong D S, *et al*. Aharonov - Bohm interference in topological insulator nanoribbons [J]. *Nature Materials*, 2010, **9**: 225 - 229.

[9] Kong D S, Rande J C, Peng H L, *et al*. Topological insulator nanowires and nanoribbons [J]. Nano Letters, 2010, **10**: 329 - 333.

[10] Kong D S, Dang W H, Cha J J, *et al*. Few-layer nanoplates of Bi_2Se_3 and Bi_2Te_3 with highly tunable chemical potential [J]. *Nano Letters*, 2010, **10**: 2245 - 2250.

[11] Hong S S, Cha J J, Kong D S, *et al*. Ultra-low carrier concentration and surface dominant transport in antimony-doped Bi_2Se_3 topological insulator nanoribbons [J]. *Nature Communications*, 2012, **3**: 757.

[12] Cha J J, Kong D S, Hong S S, *et al*. Weak antilocalization in $Bi_2(Se_xTe_{1-x})_3$ nanoribbons and nanoplates [J]. *Nano Letters*, 2012, **12**: 1107 - 1111.

[13] Tang H, Liang D, Qiu Richard L J, *et al*. Two-dimensional transport induced linear magneto-resistance in topological insulator Bi_2Se_3 nanoribbons [J]. *ACS Nano*, 2011, **5**: 7510 - 7516.

[14] Gehring P, Gao B, Burghard M, *et al*. Two-dimensional magneto-transport in Bi_2Te_2Se nanoplatelets [J]. *Applied Physics Letters*, 2012, **101**: 023116.

[15] Liu M H, Chang C Z, Zhang Z C, *et al*. Electron interaction-driven insulating ground state in Bi_2Se_3 topological insulators in the two-dimensional limit [J]. *Physical Review B*, 2011, **83**: 165440.

[16] Kim Y S, Brahlek M, Bansa N, *et al*. Thickness-dependent bulk properties and weak antilocalization effect in topological insulator Bi_2Se_3 [J]. *Physical Review B*, 2011, **84**: 073109.

[17] Chen J, He X Y, Wu K H, *et al*. Tunable surface conductivity in Bi_2Se_3 revealed in diffusive electron transport [J]. *Physical Review B*, 2011, **83**: 241304.

[18] Zhang G, Qin H, Chen J, *et al*. Growth of Topological Insulator Bi_2Se_3 Thin Films on $SrTiO_3$ with Large Tunability in Chemical Potential [J]. *Advanced Functional Materials*, 2011, **21**: 2351 - 2355.

[19] Hamdou B, Gooth J, Dorn A, *et al*. Surface state dominated transport in topological insulator Bi_2Te_3 nanowires [J]. *Applied Physics Letters*, 2013, **103**: 193107.

[20] Hikami S, Larkin A I, Nagaoka Y. Spin-orbit interaction and magnetoresistance in the two dimensional random system [J]. *Progress of Theoretical Physics*, 1980, **63**: 707.

[21] Bayot V, Piraux L, Michenaud J P, *et al*. Two-dimensional weak localization in partially graphitic carbons [J]. *Physical Review B*, 1990, **41**: 11770.

[22] Wei L M, Liu X Z, Yu G L, *et al*. Antilocalization effect in HgCdTe film [J]. *J. Infrared Millim. Waves*, (魏来明, 刘新智, 俞国林, 等. HgCdTe 薄膜的反局域效应. **红外与毫米波学报**) 2013, **32**: 141 - 144.

[23] Altshuler B L, Aronov A G. Electron-electron interaction in disordered systems [M]. New York: Elsevier Science Publishing Company, 1985.

[24] Kallaher R L, Heremans J J. Spin and phase coherence measured by antilocalization in n-InSb thin films [J]. *Physical Review B*, 2009, **79**: 075322.

[25] Rammer J, Schmid A. Destruction of phase coherence by electron-phonon interactions in disordered conductors [J]. *Physical Review B*, 1986, **34**: 1352.

[26] Reizer M Yu, Electron-phonon relaxation in pure metals and superconductors at very low temperatures [J]. *Physical Review B*, 1989, **40**: 5411.

(上接第 265 页)

[7] Jia X L, Meng Q X, Yuan C X, *et al*. A novel chiral nano structure for optical activities and negative refractive index [J]. *Optik*, 2016, **127**(14): 5738 - 5742.

[8] Schurig D, Mock J J, Justice B J, *et al*. Metamaterial electromagnetic cloak at microwave frequencies [J]. *Science*, 2006, **314**(5801): 977 - 980.

[9] Patrick R, Cumali S. Wide-band polarization independent perfect metamaterrial absorber based on concentric ring topology for solar cells application [J]. *Journal of Alloys and Compounds*, 2016, **680**: 473 - 479.

[10] Li Q, Zhang X Q, Cao W, *et al*. An approach for mechanically tunable, dynamic terahertz bandstop filters[J]. *Applied Physics A*, 2012, **107**(2): 285 - 291.

[11] Kadir O, Okan M Y, Hasan K. Metamaterial based broadband RF absorber at X-band [J]. *Int. J. Electron. Commun.* (*AEU*), 2016, **70**(8): 1062 - 1070.

[12] Wang G C, Zhang J N, Zhang B, *et al*. Photo-excited terahertz switch based on composite metamaterial structure [J]. *Optics Communications*, 2016, **374**: 64 - 68.

[13] Hu J R, Li J S, Cheng W. Research on a thermally tunable terahertz wave band-stop filter based on thermo-sensitive media[J]. *Electronic components and materials*(胡建荣, 李九生, 程伟. 基于温敏介质的温控太赫兹波带阻滤波器研究. 电子元件与材料), 2014, **33**(5): 57 - 60.

[14] Cheng W. Research on tunable terahertz wave devices using metamaterials and photonic crystals[D]. Hang zhou: China Jiliang University (程伟. 基于电磁超材料和光子晶体的可调太赫兹波器件研究. 杭州: 中国计量大学), 2014.

[15] Marcelo A B, Assis A K T. A new method for inductance calculations [J]. *J. Phys. D: Appl. Phys*, 1995, **28**(9): 1802 - 1806.

[16] Gevorgian S, Berg H. Line capacitance and impedance of coplanar-strip waveguides on substrates with multiple dielectric layers [J]. *In 31st European Microwave Conference*, 2001.

[17] Passmore B S, Allen D G, Vangala S R, *et al*. Mid-infrared doping tunable transmission through subwavelength metal hole arrays on InSb [J]. *Optics Express*, 2009, **17**(12): 10223 - 10230.

[18] Zhu J, Han J G, Tian Z, *et al*. Thermal broadband tunable Terahertz metamaterials [J]. *Optics Communications*, 2011, **284**: 3129 - 3133.

[19] Gu W H, Chang S J, Fan F, *et al*. InSb-based tunable terahertz directional beaming device [J]. *Optics Communications*, 2016, **377**: 110 - 114.